Multi-parameter optimization of a loose focusing high flux high-harmonic beamline

Kovács, K; Major, B; Balogh, E; Kőrös, Cs P; Rudawski, P; Heyl, C M; Johnsson, P; Arnold, C L; L'huillier, A; Tosa, V; Varjú, K

Published in:
Journal of Physics B: Atomic, Molecular and Optical Physics

DOI:
10.1088/1361-6455/aaff7f

2019

Document Version:
Version created as part of publication process; publisher's layout; not normally made publicly available

Multi-parameter optimization of a loose focusing high flux high-harmonic beamline

K. Kovács[1], B. Major[2,3], E. Balogh[4], Cs. P. Kőrös[3], P. Rudawski[5], C. M. Heyl[5], P. Johnsson[5], C.L. Arnold[5], A. L'Huillier[5], V. Tosa[1], K. Varjú[2,3]

[1] *National Institute for Research and Development of Isotopic and Molecular Technologies, Donat str. 67-103, 400293 – Cluj-Napoca, Romania*

[2] *ELI-ALPS, ELI-HU Non-Profit Ltd., Dugonics tér 13, Szeged 6720, Hungary*

[3] *Department of Optics and Quantum Electronics, University of Szeged, Dóm tér 9, Szeged 6720, Hungary*

[4] *Center for Relativistic Laser Science, Institute for Basic Science (IBS), Gwangju 61005, South Korea*

[5] *Department of Physics, Lund University, P.O. Box 118, SE-22100 Lund, Sweden*

Abstract

We perform a multi-dimensional parameter scan in the generation of high-order harmonics, with the main purpose to find the macroscopic conditions that optimize the harmonic yield in a specific spectral domain, around 40 eV for this particular case. The scanned parameters are the laser pulse energy, gas pressure, interaction cell position relative to focus and the cell length, while the fixed parameters are chosen to model a loose focusing configuration which is used in many existing laboratories. We performed the simulations with a 3D non-adiabatic model complemented by a detailed analysis of the phase matching mechanisms involved in an efficient harmonic generation. Based on the results we identify a range of parameter combinations that lead to a high yield in the specified spectral domain. The method and results presented here can be the framework for the design and construction of high flux high-order harmonic generation beamlines.

Keywords: high-order harmonic generation, numerical simulation, multi-dimensional parameter scan, optimization, XUV flux

1. Introduction

Since its discovery almost 30 years ago [1], high-order harmonic generation (HHG) has become a well-established and extensively studied technique to obtain coherent radiation in the extreme-ultraviolet (XUV) and even soft X-ray spectral domain. When intense ultrashort laser pulses interact with atoms in a gas medium, a highly nonlinear process, HHG takes place, and coherent XUV radiation of attosecond duration is emitted. A promising application is the investigation of electron dynamics on its natural attosecond time scale [2,3]. The importance and reliability of HHG has been demonstrated over the last few decades. The ELI-ALPS (Extreme Light Infrastructure – Attosecond Light Pulse Sources) facility uses it as the basic method for producing sources of XUV and soft X-rays [4,5].

In order to perform precise attosecond pump – attosecond probe measurements, or to induce nonlinear effects, a high flux is needed. The HHG process is highly nonlinear and has low efficiency [6,7], thus obtaining attosecond pulses at a sufficient flux [8-12] is a big challenge. A simple increase of the driving field intensity does not guarantee an increase in XUV photon flux, because i) the gas atoms in the medium may be fully ionized even before the pulse reaches its maximum, ii) the laser pulse propagates in the created plasma suffering serious distortions like intensity drop and self-phase-modulation, or iii) the phase-matching conditions are altered due to the nontrivial dependence on ionization [13]. Furthermore, continuously developing laser technology offers laser pulses at

unprecedented (peak and/or average) power. For example, the SYLOS system of ELI-ALPS will deliver <7 fs laser pulses centered at 880 nm at 1 kHz repetition rate with 4.5 TW peak power [5]. Research efforts are therefore dedicated to finding methods and configurations which could take advantage of the available high pulse powers. One possible way is to design a HHG configuration with loose focusing geometry [14] and apply the universal scaling relations for nonlinear phenomena in gases identified in Ref. [15]. The scaling principle states that if the fundamental energy increases with a factor η^2, the conversion efficiency can be preserved, if the longitudinal spatial dimensions scale as $z \rightarrow \eta^2 z$; transverse spatial dimensions scale as $r \rightarrow \eta r$ and the particle density in the medium as $\rho \rightarrow \rho/\eta^2$. These scaling laws have been analytically proven, and verified both experimentally (within the existing possibilities) and by simulations (also in cases which are beyond the currently available experimental limits), so they can rigorously guide the design of new high-flux HHG beamlines, if well optimized, smaller-scale systems are taken as the basis. There are however practical limitations of applying these rules: a 10-fold increase in the input laser pulse energy requires $\sqrt{10}$ times longer focal length for the fundamental beam and 10 times longer interaction region. Even at the new ELI infrastructures, the availability of such long lab space is limited. In addition, providing mechanical stability across these lengths is very demanding. The required focal lengths are in the range of tens of meters, see for example the data in Table 2 from Ref. [15] or the up-scaling of the existing parameters reported in [14]. Recently, tight focusing and high pressure beamlines are also considered for efficient HHG evidencing the importance of the defocusing assisted phase-matching [16,17].

Here, we report a multi-dimensional parameter scan which has as its main purpose the finding of optimized macroscopic conditions for the harmonic yield in a specific spectral domain relevant to further applications. The set of parameters which are kept fixed in this extensive study are chosen to make it possible to implement the findings in existing laboratories and research infrastructures.

The paper is organized as follows: in section 2 we present the theoretical model for HHG and the numerical implementation method. We set the basic case which is studied and the ranges for the parameters that are scanned. In section 3.1 we describe the results showing the most efficient parameter combinations. In section 3.2 we present a detailed study of two representative cases yielding high flux HHG and reveal the macroscopic mechanisms that lead to increased yield. Finally, we summarize and draw general conclusions that contain practical and useful guidelines for the design and operation of any loose focusing high-flux HHG beamline.

2. Numerical method and the multi-dimensional parameter space

Model

The calculations are performed using the adapted and extended version of the (3+1)D non-adiabatic model for pulse propagation and HHG first presented in [18], which was developed using the theory described in [19], and computational details are given in [18]. The laser pulse propagation is calculated by solving the unidirectional propagation equation that follows from the Maxwell equations, where we use cylindrical coordinates and the paraxial approximation:

$$\nabla^2 E_1(r,z,t) - \frac{1}{c^2}\frac{\partial^2 E_1(r,z,t)}{\partial t^2} = \frac{\omega_1^2}{c^2}(1-\eta_{eff}^2)E_1(r,z,t). \qquad (1)$$

The source term in the propagation equation (1) contains the laser field E_1 (of central angular frequency ω_1), therefore a self-consistent iterative method is being used to solve it. We solve the propagation equation in frequency domain, and take into account the energy loss due to ionization [20]. The effective refractive index has the form:

$$\eta_{eff}(n_a, n_e, r, z, t) = \eta_0(n_a) + \eta_2(n_0)I(r,z,t) - \frac{\omega_p^2(n_e,r,z,t)}{2\omega_1^2}, \qquad (2)$$

with the following three contributions included. (i) $\eta_0 = 1 + \delta_1 - i\beta_1$ accounts for linear refraction and absorption, which depends on the density of the neutrals n_a. (ii) The second term contains the optical Kerr effect, n_0 being the total atomic density. (iii) The third term is the dispersion due to the free electrons of density n_e, exposed with the help of plasma frequency $\omega_p = (4\pi e^2 n_e/m)^{1/2}$. The refractive index has a fast and non-trivial variation in both time and space throughout the interaction volume where HHG takes place. During the calculations, we keep track of the variation of each term, and we estimate their relative contribution and importance.

The single-atom dipole response is calculated through the Lewenstein integral [21] which gives the non-linear polarization in the strong-field approximation (SFA):

$$P_{nl}(t) = 2Re\left\{i\int_{-\infty}^{t} dt' d^*[p_{st}(t',t) - A(t)]E_1(t')exp\left[-\int_{-\infty}^{t'} w(t'')dt''\right]exp[-iS_{st}(t',t)]\cdot d[p_{st}(t',t) - A(t')]\right\}\cdot[n_0 - n_e(t)]. \qquad (3)$$

In equation (3) the physical quantities involved are the laser field (E_1), the corresponding vector potential (A), the stationary momentum (p_{st}) and action (S_{st}). Also, $w(t)$ is the ionization rate, while n_0 and n_e are the total initial and free electron densities, respectively. The bound-free transition dipole element (d) was calculated assuming a Hydrogen-like potential. The ionization rate was calculated using the modified ADK model [22].

The harmonic field E_h is constructed from the coherent addition of the atomic polarizations P_{nl}:

$$\nabla^2 E_h(r,z,t) - \frac{1}{c^2}\frac{\partial^2 E_h(r,z,t)}{\partial t^2} = \mu_0 \frac{\partial^2 P_{nl}(r,z,t)}{\partial t^2}. \qquad (4)$$

The propagation equations (1) and (4) are solved in a moving frame with c velocity and in frequency domain. The harmonic yield in a given spectral domain $[q_1,q_2]$ is finally obtained as a power spectrum by radially integrating the Fourier transform of the harmonic field:

$$\int_{q_1}^{q_2}\int_0^R [E_h(\omega,r)]^2 r dr d\omega \qquad (5)$$

A time-dependent phase-matching calculation is also implemented as an additional tool in the model. According to the classical phase-matching theory [23] the wave vector mismatch is the difference between the wave vector of the q^{th} order propagated harmonic and the q^{th} order polarization wave vector $\delta k(t) = q\frac{2\pi}{\lambda} - |\boldsymbol{k}_{pol}(t)|$, where

$$\boldsymbol{k}_{pol}(r,z,t) = q\{n_q(2\pi/\lambda)e_z + \nabla arg[E_1(r,z,t)]\} + \nabla\alpha I(r,z,t). \qquad (6)$$

The q^{th} order polarization accounts for the neutral dispersion of the q^{th} order harmonic (through n_q in the first term) and inherits the phase properties of the driving pulse (second term), where e_z is the unit vector along z axis. It also includes the effect of the atomic dipole phase (last term), which is proportional to the intensity gradient of the propagated pulse. Our model describes phase matching in

a time-dependent form [13], where the phase of the *propagated* field is taken into account, and the intensity is the cycle-averaged value around a given optical cycle and in a given *(r,z)* spatial position.

The model has been implemented in a computer code developed in order to meet the requirements of various experimental conditions. For example, the code has been tested and validated against experiments like: HHG in two- (and multiple-) color configurations [24-27], testing the scaling principles [15], evidencing the important role of macroscopic effects in HHG such as ionization and phase-matching [28-30]. Therefore, the model enables us to perform numerical "experiments" to optimize the HHG arrangement prior to experimental implementation. The input parameters are experimentally measurable, or can be estimated: (1) laser pulse properties like beam type (e.g. Gaussian, Bessel, etc.), pulse energy, central wavelength, duration, chirp, waist size; (2) generation geometry like focal length, iris size (if any) and position, cell position, far field focusing; (3) medium information like gas type, pressure (distribution if not uniform), cell (or jet) length.

The model provides results that are experimentally measurable. For example, the high-order harmonic power spectra or individual harmonics divergence can be directly compared with experimental spectra. Further, in the calculations we can time-resolve down to the optical half-cycle level the deformations of the driving pulse through propagation, and identify specific optical cycles in which individual harmonics are emitted. In the spatial domain, we can follow the variation of the driving pulse's peak intensity and shape. We can track the spatial build-up of selected harmonic orders and thus have information about the underlying phase-matching mechanisms. These time- and space-resolved information are not experimentally available and therefore can be of great help in elucidating the basic physical phenomena that contribute to the measurable macroscopic results.

A recent improvement of the model is the implementation of multiple ionization processes [31]. This step was important because laser technology has evolved and very high intensity ultrashort pulses are routinely available in many research laboratories, allowing ionization of atoms beyond the least bound electron. We take into account sequential ionization governed by a set of rate equations [32], and integrate the polarizations generated by the ionic species. However, in this study we only account for the polarization generated by the neutrals.

Fixed parameters

We choose pulse duration of 10 fs, a central wavelength of 800 nm and a focal length of 21 m. The radius ($1/e^2$ intensity) of the beam waist at the focusing element is 30 mm. With these parameters kept unchanged the Rayleigh range of the beam is 12.5 cm and the focused beam diameter is 360 μm. The total length of the interaction region is 20 cm, the gas medium being argon. The distance from near- to far-field is 6 m, and the threshold for divergence is 10 mrad, meaning that harmonic components with higher divergence are discarded.

Scanned parameters

These are the laser pulse energy (3 mJ, 11.6 mJ); gas pressure (0.1, 0.38, 1.41, 5.31, and 20 mbar); cell entrance position with respect to the focus (-50; -25 -10, 0, 10; 25; and 50 cm) and cell length (4, 8, 12, 16, and 20 cm). In the simulations the gas medium was assumed to have constant pressure. In several selected cases we performed the calculations by assuming smoothly increasing pressure

adding 2 mm long wings at both cell ends. The results were essentially the same with and without pressure wings. We performed simulations in the 4-dimensional parameter space and obtained a total of 350 spectra. The schematic representation of the geometrical arrangement along the propagation axis is shown in Fig. 1. Although the extreme positions +/-50 cm are at $4z_R$ distance from the focus, we found that the results are of practical importance and therefore we include them in the analysis.

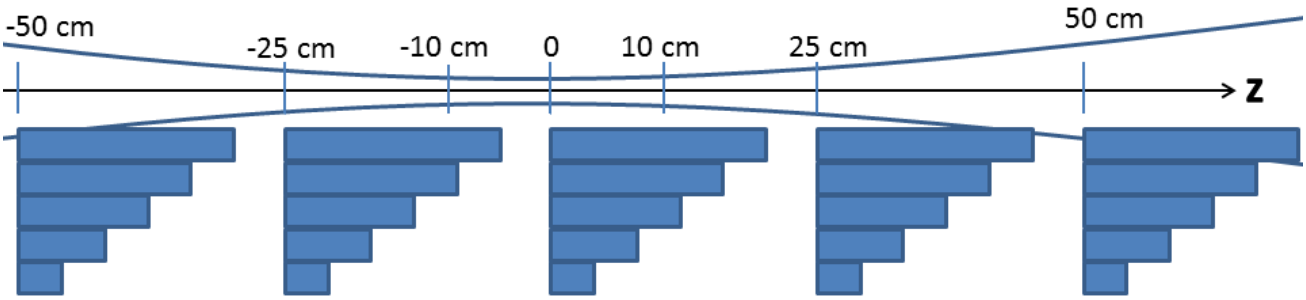

Fig. 1. Schematic view of the geometrical arrangements. The gas cell entrance position was scanned in the [-50; +50] cm interval as shown by ticks. The medium length as varying parameter is visualized through the blue rectangles of increasing length.

3. Results and discussion

3.1. Parameter sub-space leading to highest conversion efficiency

The main purpose of this multi-dimensional parameter scan is to find the combination which maximizes the harmonic yield around 40 eV. We chose to optimize the yield for this spectral range because it is in the plateau of the Ar harmonic spectrum, it lies before the Cooper minimum (around 50-55 eV [33]) and has high enough photon energy to be interesting for attosecond electron dynamics studies.

From the multitude of calculated power spectra we extract in the first step a map of maximum yield (Fig. 2). All spectra are in the same (arbitrary) units, directly comparable with each other. Moreover, the *relative yields* are in accordance with the expected experimental outcome. Therefore, when we find (one or more) optimal macroscopic configuration(s) for maximum harmonic yield, this is a reliable indication for the experimental parameter set to be implemented. In Fig. 2 we show two maps with the parameter ranges where simulations indicate a maximum harmonic yield for the 25th harmonic. One scanned parameter is the length of the gas medium which is easily included in the simulations because while advancing with the propagation we calculate the near-field HHG power spectrum every 4 cm in the 20 cm long cell. In Fig. 2 we present the maximum value of the harmonic yield observed at any position throughout the medium. We prefer to represent the logarithm of the harmonic yield and consider that the parameters are close to the optimum if the obtained harmonic yield is within one order of magnitude. The highest values calculated for the two input laser pulse energies are indicated by circles in Fig. 2. Below we analyze the mechanism of harmonic build-up and discuss on the optimal length of the gas medium.

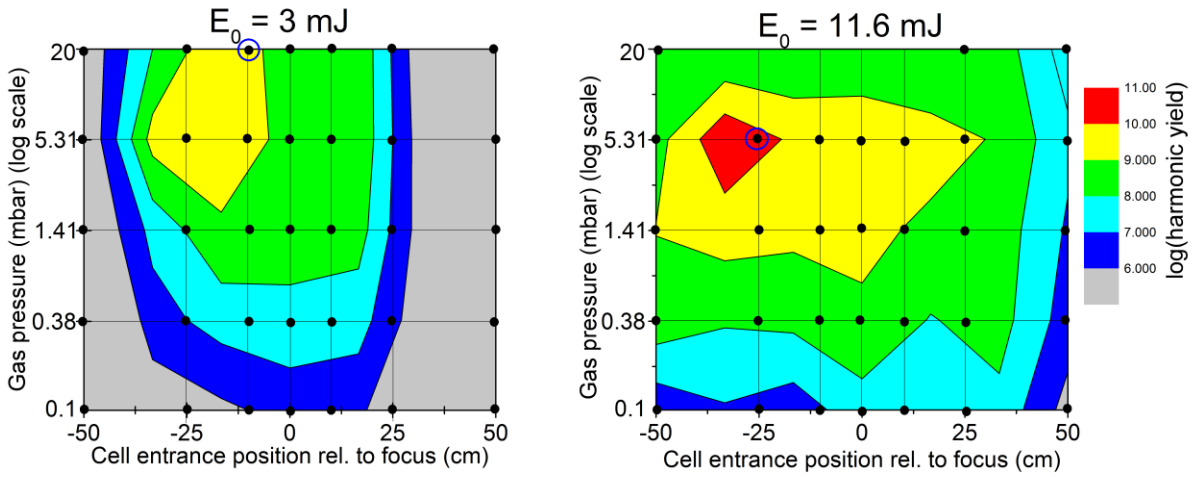

Fig. 2. Maps of the logarithm of maximum harmonic yield vs cell entrance positions and gas pressure map. Dots represent the exact location of the data points between which interpolation was performed. We represent the maximum obtainable yield within the 20 cm long argon medium, thus the optimum length can vary from point to point in this representation. The optimum cell length is discussed in the text and represented in Fig. 3. The highest values are indicated by circles.

From both panels of Fig. 2 it is obvious that a higher efficiency is obtained when the gas medium is placed before the laser focus, a result which was first attributed to self-guiding [18,34]. The harmonic yield obtained with the higher pulse energy (11.6 mJ) is in general one order of magnitude larger than that obtained using the 3 mJ pulse, as expected. At the highest laser energy the best yield is obtained when the generating medium is placed $2z_R$ before the focus. The reason is that the intensity in the medium is high enough to fully deplete the neutrals in the leading edge. The pulse suffers serious distortions, and the conditions for efficient HHG are not met. The optimal parameter combinations are (3 mJ; 20 mbar; -10 cm) and (11.6 mJ; 5.31 mbar; -25 cm). These two cases will be explored in more detail in the next subsection in order to clarify both the microscopic and macroscopic mechanisms that enable the increase of harmonic yield. The maps in Fig. 2 also carry encouraging information: even if in the real experiments one cannot tune the system to the exact optimal parameters, yet in the vicinity of the best parameter combination there is still high efficiency. For the 3 mJ pulse energy in the parameter subspace (5.31 mbar; 20 mbar) x (-25 cm; -10 cm) the yield is still within one order of magnitude of the maximum. The conditions are even more relaxed for the higher pulse energy (11.6 mJ) group. In the large subspace of parameters (1.41 mbar; 5.31 mbar) x (-50 cm; +10 cm) a high flux of the harmonics around 40 eV is obtained.

In Fig. 3 we show which gas cell length gives the highest efficiency. This represents the fourth scanned parameter. The importance of the medium length as experimental parameter can be understood by the physics of the HHG process. It is known that phase matching modulates the HHG efficiency [35]. Therefore it is important to correctly estimate the combined influence of medium length, coherence length and absorption length [36] for the harmonics of interest, and then to adjust the medium length in order to maximize the attainable XUV photon number. As expected, there is a clear trend: at low gas density and for a cell placed before the laser focus the harmonic yield keeps growing up to 20 cm, which is the longest cell used in the simulations. As the pressure increases,

reabsorption of the generated XUV becomes dominant and causes a drop in efficiency after a certain distance of propagation. We will discuss this aspect for the two representative cases.

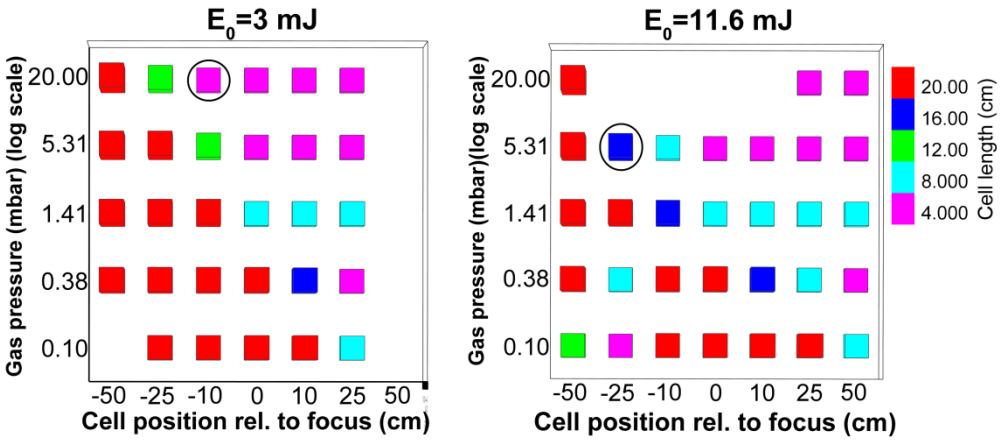

Fig. 3. Chart of the optimum cell length (cm), indicated by the color of the squares, as a function of gas pressure and cell entrance position relative to focus for the two cases of pulse energies 3 mJ (left) and 11.6 mJ (right). We indicate by circles the two representative cases which will be discussed.

3.2. Detailed study of representative high efficiency cases

In order to elucidate the mechanisms governing the harmonic radiation build-up, we present in detail two representative cases. Case **A (3 mJ; 20 mbar; -10 cm)** which gives the most efficient yield of the parameter space for the 3 mJ pulse energy and case **B (11.6 mJ; 5.31 mbar; -25 cm)** which produces the highest yield around 40 eV for the 11.6 mJ pulse energy. The absolute yield in the second case is almost one order of magnitude higher than the highest obtained with a pulse of 3 mJ initial energy and it is the maximum in the whole explored parameter space. In terms of efficiency, this means a factor of two enhancement, however we emphasize the absolute yield instead, because this is the important quantity when the generated attosecond pulses are further used in experiments. In our study presented below, we follow step by step the pulse propagation and its temporal distortions on the optical cycle level as well as the modifications of its radial profile and we investigate the harmonic radiation build-up and the different phase-matching mechanisms involved. All the figures presenting the results from this point on are labeled with **A (3 mJ; 20 mbar; -10 cm)** and **B (11.6 mJ; 5.31 mbar; -25 cm)** below. A geometrical sketch is presented in Fig. 4 showing the cell positions with respect to the Rayleigh length. The position in each cell where the maximum harmonic yield is obtained is also indicated by a vertical line.

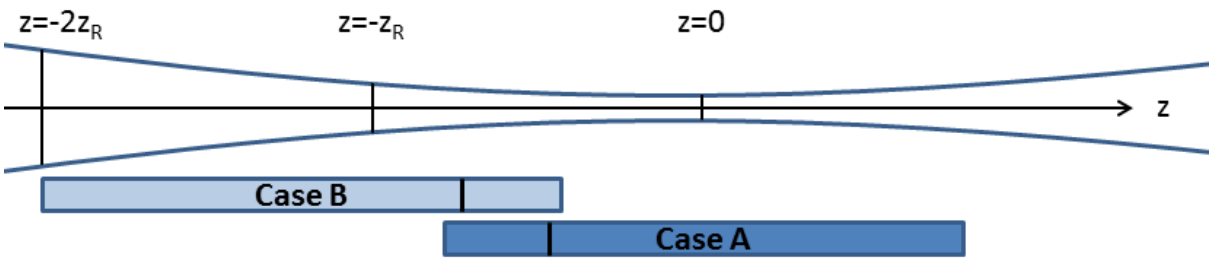

Fig. 4. Geometrical arrangement of the two cases analyzed in detail. We indicate the position of maximum yield within the cells.

In Fig. 5 we present the total power spectra recorded in the two configurations. The spectra are radially integrated and contain the contributions from the off-axis radiation up to 10 mrad divergence. The harmonic spectrum is the most important outcome of an experiment and carries information about the whole system. The pulse peak intensity at the entrance of the cell is $3.4 \cdot 10^{14}$ W/cm^2 in case **A** and $4 \cdot 10^{14}$ W/cm^2 in case B. According to the cutoff law, this would correspond to cutoff orders q_{max}=51, and q_{max}=59 respectively. We conclude that the simulated high-harmonic cutoffs are much reduced (being $q_{cut} \approx 31$) and do not differ significantly in the two cases. Near-field spectra give a clear indication of the optimal cell length for the given parameter configuration. The charts of Fig. 3 indicate that high pressures are associated with shorter efficient medium [36], which is confirmed in both cases. After 4 cm of propagation the yield in case **A** is higher than the yield of case **B**, but as propagation proceeds, the build-up of harmonic radiation is completely different in cases **A** and **B**, which suggests different phase-matching mechanisms. We also recall the different propagation regimes for the two configurations. Case **A** is symmetrical with respect to the focus and fits entirely within $\pm z_R$. In case **B,** the cell begins at $-2z_R$ and ends before the geometrical focus. Case B is a configuration providing high harmonic yield due to the combination of high input laser pulse energy and the interaction region beginning at $-2z_R$ position. The laser intensities at the entrance of the medium are quite close for the two cases and are higher than the threshold value necessary for the formation of self-guiding in argon medium ($2\text{-}3 \cdot 10^{14}$ W/cm^2) [18,34,37]. However there are also other criteria for propagation in self-guided mode, which are met only in case B, not in case A, as we will discuss below.

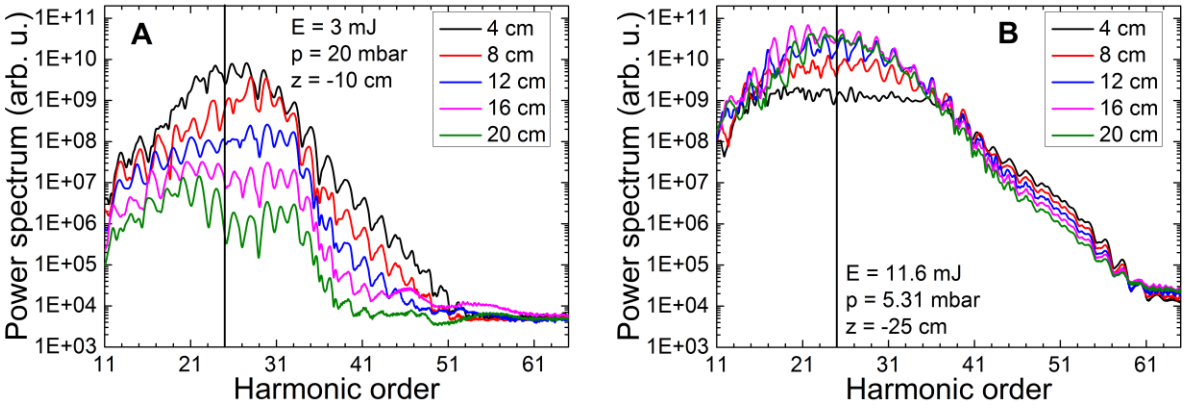

Fig. 5. Radially integrated power spectra of the two representative cases. Near-field spectra were taken at every 20% of propagation distance in the Ar medium.

In the following we present in detail case A, explain the mechanisms involved and the methods used, while for case B we highlight the differences compared to case A.

3.2.1 Case A

In Fig. 6 (a) we show the spatial *(z, r)* evolution of: the driving pulse's peak intensity. H25 is the cutoff order at $1.2 \cdot 10^{14}$ W/cm^2, therefore below this value no dipole radiation is emitted. For this reason, in Fig. 6 (a) the lowest represented intensity value is 1.2 10^{14} W/cm^2 (dark blue). The spatial

build-up of harmonic H25 is shown in Fig. 6 (b). The coherence length map for H25, calculated with the time-independent method from Ref. [23], is represented in Fig. 6 (c)

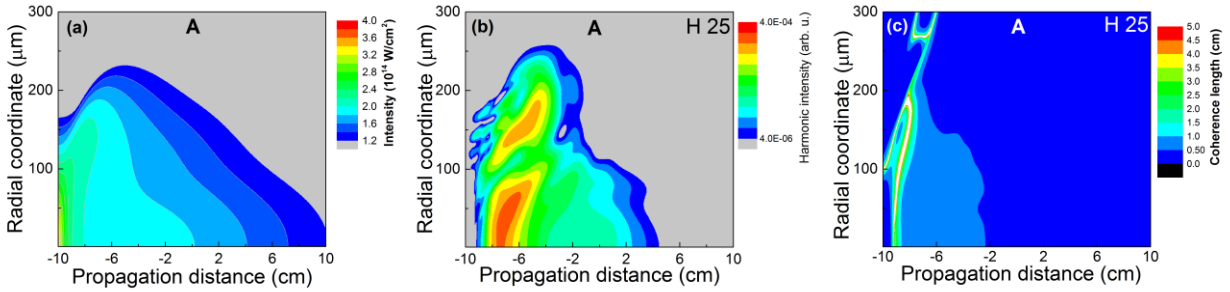

Fig. 6.(a) Spatial evolution of the driving pulse's peak intensity (linear scale in 10^{14} W/cm^2 units). (b) Spatial build-up of harmonic H25 i.e. 39 eV (logarithmic scale, spans two orders of magnitude, arbitrary units). (c) Coherence length map calculated with the static model of Balcou [23] (linear scale, in cm).

In Fig 6 (a) the initial ionization level is 43% on-axis which causes rapid defocusing of the beam, although the medium is placed before focus. Defocusing results in intensity decrease, even before the focus below the threshold necessary for the onset of refocusing or self-guiding propagation [18,34,37]. After the focus, the geometrical defocusing is added and the pulse peak intensity continuously decreases. The situation off-axis is slightly different only at the very beginning of the propagation: due to the initially lower intensity and lower ionization level (~10% at 100 μm off-axis), the initial defocusing is also slower and leads to the formation of a shoulder in the intensity map. This axial-radial modification of the laser pulse intensity produces an intensity-gradient which is favorable for the constructive build-up of HHG radiation in the spectral domain around 40 eV in the first quarter of the cell. This type of off-axis phase-matching is observed in Fig. 6 (b) where we show the spatial build-up of H25. Due to the fact that the phase-matching volume extends radially up to 250 μm off-axis in the first quarter of the generation medium, these off-axis radiation components give a significant contribution to the radially integrated power spectrum, as shown in Fig. 5. The coherence length evolution in Fig. 6 (c) supports the previous discussion, because it confirms that harmonic H25 is generated with long coherence length at the beginning of the propagation length, and this extends radially to 200 μm. We emphasize here that the method for wave-vector mismatch (Δk) calculation (see Eq. 6) is independent of the dipole calculation (Eq. 3) and depends only on the intensity and phase of the *propagated* laser field. It has therefore the role of an independent check or validation method when we discuss about different "phase-matching effects".

The simulation code also gives the opportunity to follow the temporal dynamics of the laser pulse propagation and HHG. In Fig. 7 (a) we show the temporal shape of the laser pulse at the beginning of the propagation and at the distance of maximum yield, on-axis (*z=-6cm; r=0*). Simultaneously, we also show the temporal dynamics of the ionization through the pulse. The shaded area indicates the temporal window in which optical cycles the high-harmonic radiation is emitted under good phase-matching conditions. We mention, however, that the main contribution to the harmonic yield comes from the off-axis phase-matched radiation (see Fig. 7 (b)), therefore the analysis only on-axis is not sufficient to fully capture the harmonic build-up mechanism. It is illustrative, however, for assessing the degree of distortion that an initially Gaussian few-cycle pulse can undergo during propagation: (i)

strong self-phase modulation in those early optical cycles where the ionization dynamics is fast and causes the rapid variation of the medium's refractive index; (ii) intensity decrease due to defocusing caused mainly by the created plasma. The quantity being responsible for the intensity drop is the density of free electrons (n_e=pressure x ionization_fraction), rather than solely the ionization level.

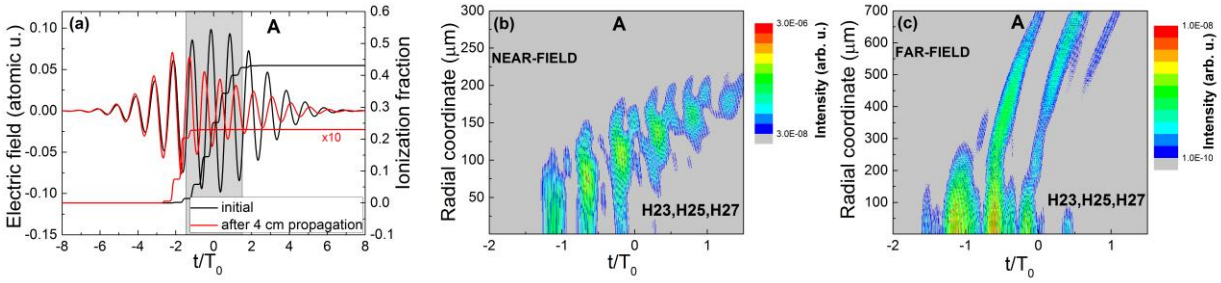

Fig. 7. (a) Temporal shape of the laser pulse and the corresponding ionization rate – on-axis. Black lines are the initial values, red lines are at the cell length where maximum harmonic yield was obtained. The ionization level is initially 43% and drops to 2.3 % after 4 cm of propagation. The shaded area indicates the time domain when the harmonics of interest are generated. (b) Temporal-radial profile of harmonics from H23 to H27.The map is taken in the near-field at the cell length of maximum yield. (c) The same as in (b) in the far-field.

Due to the observation that off-axis generation contributes with the largest weight to the spectral power (see Fig. 6 (b)), it is important to examine also the temporal-radial structure of the harmonic field. In Fig. 7 (b) we show the temporal-radial profile of harmonics from H23 to H27 at the optimum propagation length. Our spectral domain extends +/- one laser photon energy beyond the nominal harmonic orders to capture possible red or blue shifts. The maps confirm the significant contribution of the off-axis radiation. Strongest attosecond pulses are constructed in two optical cycles preceding the nominal pulse center. The relevant optical cycles are highlighted in grey in Fig. 7 (a).

Although the near-field map in Fig. 7 (b) indicates the presence and importance of the off-axis harmonic emission, this map does not give information about the divergence of the harmonic radiation. In Fig. 7 (c), we present the far-field distribution of the harmonic field obtained by Hankel-transform to a location 6 m downstream. The harmonic signal has the highest brightness mostly on-axis and close-to-axis. This aspect is counter-intuitive at the first sight. The selected harmonics are emitted predominantly off axis, as seen in the near-field picture, but under very similar circumstances: they are emitted in the same few optical cycles, with similar phases. The whole interaction region has cylindrical symmetry, and in the far-field (close to) on-axis these emissions interfere constructively because they travelled equal optical paths. The fact that – beside high efficiency – the harmonic radiation has also good optical quality is a bonus, because this feature is really difficult to control. In this way, the whole generated harmonic signal can be detected and used in further experiments.

Case A is situated at the border of the explored parameter space, which could suggest that the best yield is beyond the applied parameter combinations. Keeping the parameters unchanged, but calculating the harmonic yield after every 1 cm of propagation, we can confirm that the highest yield is found after 4 cm of field propagation. We also checked for the optimal pressure: for a run with 40 mbar pressure, keeping other parameters unchanged, the yield drops one order of magnitude.

3.2.2. Case B

Fig. 8 represents the propagation of the fundamental and harmonic 25 in case B. Comparing Fig. 6 (a) and Fig. 8 (a), we observe that in both cases the initial laser intensity drops in the first quarter of the cell.

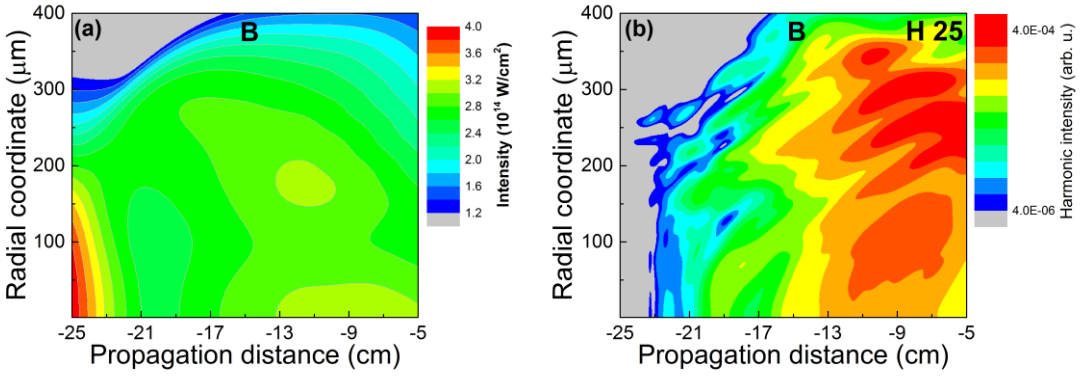

Fig. 8.(a) Spatial evolution of the driving pulse's peak intensity (linear scale in 10^{14} W/cm^2 units). (b) Spatial build-up of harmonic H25 i.e. 39 eV (logarithmic scale, spans two orders of magnitude, arbitrary units).

The initial ionization level is 61% which causes the initial defocusing and decrease of the pulse intensity. However, in contrast to case A, the on-axis pulse intensity does not fall below $2.5 \cdot 10^{14}$ W/cm^2, allowing for beam refocusing effects. The general situation off-axis is similar, with an "island" of slight refocusing which is important for the phase-matched generation of harmonic 25, as shown in Fig. 8 (b). In this configuration harmonics build up continuously in the interaction volume, attaining the maximum yield at 80% of the propagation length. Indeed, the absorption length of the 40 eV radiation in 5.31 mbar argon is L_{abs}=23 mm. According to Constant et al. [36] the emitted radiation saturates after ~8L_{abs} which in this case is 18 cm. For this particular configuration we extended the simulation up to 40 cm interaction length. The results were in agreement with the theory [36], the harmonic signal decreases after the optimum length of 16-18 cm. The high yield is also provided by the radial extension of the phase-matching region up to 350 μm. In this particular configuration we encounter a conventional non-collinear phase-matching with quadratic growth of the yield until saturation, which is expected when the gas medium is placed before the laser focus [23,34].

In order to understand the mechanism behind phase matching in case B, we use the time-dependent model as described in [13,30]. In those cases when the phase and/or intensity of the driving field changes significantly in successive optical cycles, also the dipole radiation is emitted with a different phase, and this is what we observe in case B. In Fig. 9 we show the spatial coherence length maps at different time instants during the laser pulse. The maps show regions of long coherence length (in white) which move farther off-axis in successive optical cycles. The same temporal-radial characteristic features should also be observed in the propagated harmonic field.

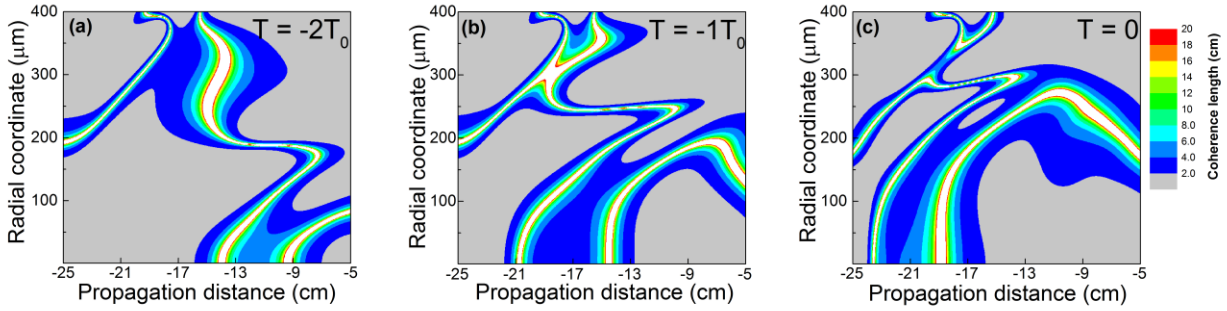

Fig. 9. Time-dependent coherence length maps of H25: (a) T=-2T_0; (b) T=-1T_0; (c) T=0, T_0 being the laser optical cycle. Color map has linear scale, cm units.

In Fig. 10 (a) we show the temporal shape of the driving laser pulse. As expected, due to the higher initial intensity the distortion of the fundamental pulse is more pronounced than in case A. Self-phase modulation is very strong in those early optical cycles where the ionization dynamics are fast. As a consequence, the pulse is almost split in time. The highest pulse intensity is thus moved to very early optical cycles (-5T_0 to -3T_0), but the field (amplitude and phase) variation is so strong that dipoles emitted in these cycles cannot build up constructively. The optical cycles which turn out to be relevant for efficient HHG are around the nominal pulse center (-2T_0 to +1T_0), highlighted in grey in Fig. 10 (a). For these optical cycles the ionization front is over, therefore the medium's refractive index does not change in time, providing good phase-matching conditions. Fig. 10 (b) shows the temporal-radial map of harmonics 23 to 27 in the near-field, at the propagation distance where the maximum yield is obtained, i.e. at z=-9 cm, after 16 cm of propagation. Fig. 10 (b) is obtained by taking a snapshot at a particular *z* position as a function of *r* within a given time window. The most intense spots at -2T_0, -1T_0 and 0 time instants are at ~100 μm, 200 μm and 300 μm off-axis, respectively. These are in good agreement with the long coherence length regions observed in the respective maps of Fig. 9. The harmonic build-up is strongly influenced by the propagation of the fundamental field (see Eq. 6.). Fig. 10 (b), for example, shows the effect of the plasma cone, which gradually evolves off axis. The shape of equal intensity becomes a cone, which is the origin of the strong harmonic emission gradually moving farther off-axis.

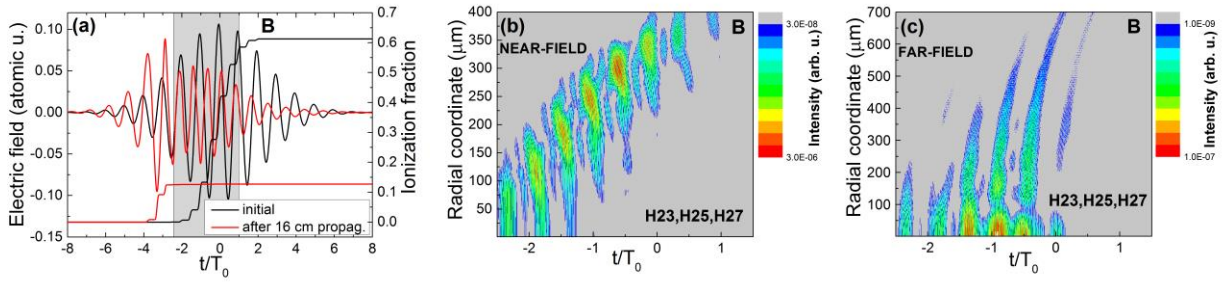

Fig. 10. (a) Temporal shape of the laser pulse and the corresponding ionization fraction – on-axis. Black lines are the initial values, red lines are at the cell length where maximum harmonic yield was obtained (after 16 cm propagation at z=-9 cm). The shaded area spans the time domain when the harmonics of interest are generated. (b) Temporal-radial profile of harmonics from H23 to H27. The map is taken in the near-field at the cell length of maximum yield. (c) The same as in (b) in the far-field.

Fig. 10 (c) shows the harmonic far-field distribution 6 m downstream. Most of the radiation is concentrated in the close vicinity of the optical axis and therefore exhibit the same coherence characteristics as in case A.

4. Conclusions

In this paper we presented the main results of an extended multi-dimensional parameter scan for a loose focusing HHG scheme. The main goal of this study was to find the best parameter combination for the highest attainable harmonic yield, with potential implementation and application in the ELI-ALPS facility after upscaling [4]. The results obtained from the simulations give a useful estimation of the *relative* photon yield in different parameter configurations.

The multi-dimensional parameter scan was done along four parameters, namely the input laser pulse energy, argon gas pressure, cell position relative to focus and cell length. The input properties of the laser pulse and the focusing geometry were kept constant. As a main general outcome of the study, we can conclude that there is a well-defined parameter subspace where we found optimal high-order harmonic yield for the XUV spectral domain around 40 eV. Specifically, the interaction of 10 fs, 800 nm Gaussian pulse loosely focused (f = 21 m) into argon gas resulted in very high photon yield at 40 eV for: 11.6 mJ pulse energy, 1.41 mbar to 5.31 mbar pressure, and -50 cm to +10 cm cell position relative to focus. The optimum cell length depends mainly on the absorption length of the XUV radiation in the specific configuration.

We presented in detail two cases from the investigated parameter space in which we analyzed the temporal and spatial variation of the driving laser pulse during propagation, performed time-dependent phase-matching calculations, and analyzed the generated high-order harmonic radiation in the spectral, spatial, and temporal domain. The results obtained with the full 3D calculations and with the phase matching model mutually support each other, offering a good understanding of the HHG process.

The theoretical and numerical methods used here provide a set of useful tools in modeling and designing gas-HHG experiments. Applying the scaling laws for the laser pulse energy [15] the results of the simulations presented in this paper can be widely used as practical guidelines for planning and construction of high efficiency gas-HHG beamlines. As a confirmation of the usefulness of a multi-dimensional parameter scan combined with the general scaling principles [15] we mention that scaling up the parameters of case B from this study (i.e. optimum yield) we obtain exactly the SYLOS LONG beamline parameters at ELI-ALPS, namely 100 mJ pulse energy, 63 m focusing and 2 m long gas target.

Acknowledgements

KK and VT acknowledge support from the Romanian National Authority for Scientific Research and Innovation, CNCS-UEFISCDI project RO-CERN 03ELI (PROPW). Simulations were performed in the Data Center of INCDTIM Cluj-Napoca. PR, CMH, PJ, CLA and ALH acknowledge support from the Swedish Research Council, the European Research Council (advanced grant PALP), the Knut and Alice Wallenberg Foundation and the Swedish Foundation of Strategic Research. The ELI-ALPS project (GINOP-2.3.6-15-2015-00001) is supported by the European Union and co-financed

by the European Regional Development Fund. We acknowledge KIFÜ for awarding us access to supercomputing resources based in Hungary at Debrecen and at Szeged.

References

[1] M. Ferray, A. L'Huillier, X. F. Li, G. Mainfray, and C. Manus, *Multiple-harmonic conversion of 1064 nm radiation in rare gases*, J. Phys. B **21**, L31 (1988).

[2] F. Krausz and M. Ivanov, *Attosecond physics*, Rev. Mod. Phys. **81**, 163-234 (2009)

[3] F. Calegari, G. Sansone, S. Stagira, C. Vozzi, and M. Nisoli, *Advances in attosecond science*, J. Phys. B: At. Mol. Opt. Phys. **49**, 062001 (2016)

[4] S. Kühn et al., *The ELI-ALPS facility: the next generation of attosecond sources*, J. Phys. B: At. Mol. Opt. Phys. **50** 132002 (2017)

[5] R. Budriūnas, T. Stanislauskas, J. Adamonis, A. Aleknavičius, G. Veitas, D. Gadonas, S. Balickas, A. Michailovas, and A. Varanavičius, *53 W average power CEP-stabilized OPCPA system delivering 5.5 TW few cycle pulses at 1 kHz repetition rate*, Optics Express **25** (5) 5797-5608 (2017) See http://eli-alps.hu

[6] J. Tate, T. Auguste, H. G. Muller, P. Salières, P. Agostini, and L. F. DiMauro, *Scaling of Wave-Packet Dynamics in an Intense Midinfrared Field*, Phys. Rev. Lett. **98**, 013901 (2007)

[7] A. D. Shiner, C. Trallero-Herrero, N. Kajumba, H.-C. Bandulet, D. Comtois, F. Légaré, M. Giguère, J-C. Kieffer, P. B. Corkum, and D. M. Villeneuve, *Wavelength Scaling of High Harmonic Generation Efficiency*, Phys. Rev. Lett. **103**, 073902 (2009)

[8] B. Manschwetus et al., *Two-photon double ionization of neon using an intense attosecond pulse train*, Phys. Rev. A **93**, 061402(R) (2016)

[9] P. Tzallas, D. Charalambidis, N. A. Papadogiannis, K. Witte, and G. D. Tsakiris, *Direct observation of attosecond light bunching*, Nature (London) **426**, 267 (2003)

[10] Y. Nabekawa, H. Hasegawa, E. J. Takahashi, and K. Midorikawa, *Production of Doubly Charged Helium Ions by Two-Photon Absorption of an Intense Sub-10-fs Soft X-Ray Pulse at 42 eV Photon Energy*, Phys. Rev. Lett. **94**, 043001 (2005)

[11] E. J. Takahashi, P. Lan, O. D. Mücke, Y. Nabekawa, and K. Midorikawa, *Attosecond nonlinear optics using gigawatt-scale isolated attosecond pulses*, Nat. Commun. **4**, 2691 (2013)

[12] P. Tzallas, E. Skantzakis, L.A.A. Nikolopoulos, G.D. Tsakiris, and D. Charalambidis, *Extreme-ultraviolet pump-probe studies of one-femtosecond-scale electron dynamics*, Nat. Phys. **7**, 781 (2011)

[13] V. Tosa, H. T. Kim, I. J. Kim, and C. H. Nam, *High-order harmonic generation by chirped and self-guided femtosecond laser pulses. I. Spatial and spectral analysis; II. Time-frequency analysis*, Phys Rev. A **71**, 063807 and 063807 (2005)

[14] P. Rudawski, C. M. Heyl, F. Brizuela, J. Schwenke, A. Persson, E. Mansten, R. Rakowski, L. Rading, F. Campi, B. Kim, P. Johnsson, and A. L'Huillier, *A high-flux high-order harmonic source* Review of Scientific Instruments **84**, 073103 (2013)

[15] C. M. Heyl, H. Coudert-Alteirac, M. Miranda, M. Louisy, K. Kovács, V. Tosa, E. Balogh, K. Varjú, A. L'Huillier, A. Couairon, and C. L. Arnold, *Scale-invariant nonlinear optics in gases*, Optica **3**, 75 (2016)

[16] A. S. Johnson, D. R. Austin, D. A. Wood, Ch. Brahms, A. Gregory, K. B. Holzner, S. Jarosch, E. W. Larsen, S. Parker, Ch. S. Strüber, P. Ye, J. W. G. Tisch, J. P. Marangos, *High-flux soft x-ray harmonic generation from ionization-shaped few-cycle laser pulses*, Sci. Adv. **4**, eaar3761 (2018)[17] C. Jin, M-C. Chen, H-W. Sun, C. D. Lin, Extension of water-window harmonic cutoff by laser defocusing-assisted phase matching, Opt. Lett 43 (18), 4433-4436 (2018)

[18] E. Takahashi, V. Tosa, Y. Nabekawa, K. Midorikawa, *Experimental and theoretical analyses of a correlation between pump-pulse propagation and harmonic yield in a long-interaction medium*, Phys. Rev. A **68**, 023808 (2003)
[19] E. Priori, G. Cerullo, M. Nisoli, S. Stagira, S. De Silvestri, P. Villoresi, L. Poletto, P. Ceccherini, C. Altucci, R. Bruzzese, and C de Lisio, *Nonadiabatic three-dimensional model for high-order harmonic generation in the few-optical-cycle regime*, Phys. Rev. A **61**, 063801 (2000)
[20] M. Geissler, G. Tempea, A. Scrinzi, M. Schnürer, F. Krausz, and T. Brabec, *Light Propagation in Field-Ionizing Media: Extreme Nonlinear Optics*, Phys. Rev. Lett **83**, 2930-2933 (1999)
[21] M. Lewenstein, Ph. Balcou, M. Yu Ivanov, A. L'Huillier, P.B. Corkum, *Theory of high-harmonic generation by low-frequency laser fields*, Phys. Rev. A **49**, 2117 (1994)[22] X. M. Tong and C. D. Lin, *Empirical formula for static field ionization rates of atoms and molecules by lasers in the barrier-suppression regime*, J. Phys. B: At. Mol. Opt. Phys. **38** 2593–2600 (2005)
[23] Ph. Balcou, P. Salières, A. L'Huillier, and M. Lewenstein, *Generalized phase-matching conditions for high harmonics: The role of field-gradient forces*, Phys. Rev. A **55**, 3204-3210 (1997)
[24] E. Balogh, B. Bodi, V. Tosa, E. Goulielmakis, K. Varju, P. Dombi, *Genetic optimization of attosecond-pulse generation in light-field synthesizers*, Phys. Rev. A **90**, 023855 (2014)
[25] M. Negro et al., *Non-collinear high-order harmonic generation by three interfering laser beams*, Opt. Express **22**, 29778-29786 (2014)
[26] B. Schütte et al., *Bright attosecond soft X-ray pulse trains by transient phase-matching in two-color high-order harmonic generation*, Opt. Express **23**, 33947-33955 (2015)
[27] M. Negro et al., *Gating of high-order harmonics generated by incommensurate two-color mid-IR laser pulses*, Las. Phys. Lett. **8**, 875-879 (2011)
[28] V. Tosa, K.T. Kim, C.H. Nam, *Macroscopic generation of attosecond-pulse trains in strongly ionized media*, Phys. Rev. A **79**, 043828 (2009)
[29] C. Jin et al., *Separation of target structure and medium propagation effects in high-harmonic generation*, J. Phys. B At. Mol. Opt. Phys. **44**, 095601 (2011)
[30] C. Vozzi, M. Negro, F. Calegari, S. Stagira, K. Kovacs, V. Tosa, *Phase-matching effects in the generation of high-energy photons by mid-infrared few-cycle laser pulses*, New J. Phys. **13**, 073003 (2011)
[31] V. Tosa, K. Kovács, D. Ursescu, K. Varjú, *Characteristics of femtosecond laser pulses propagating in multiply ionized rare gases*, Nucl. Instr. Meth. Phys. Res. B **408**, 271-275 (2017)
[32] V. Tosa, K. Kovács, B. Major, E. Balogh, K. Varjú, *Propagation effects in highly ionized gas media*, Quant. El. **46**, 321-326 (2016)
[33] J. Higuet et al., *High-order harmonic spectroscopy of the Cooper minimum in argon: Experimental and theoretical study*, Phys. Rev. A **83**, 053401 (2011)
[34] H.T. Kim, I.J. Kim, V. Tosa, Y.S.Lee, C.H. Nam, *High brightness harmonic generation at 13 nm using self-guiding and chirped femtosecond laser pulses*, Appl. Phys. B **78** 863-867 (2004)
[35] S. Kazamias, D. Douillet, C. Valentin, F. Weihe, F. Augé, Th. Lefrou, G. Grillon, S. Sebban, and Ph. Balcou, *Observation of high-contrast coherence fringes in high-order harmonic generation*, Phys. Rev. A **68**, 033819 (2003)
[36] E. Constant, D. Garzella, P. Breger, E. Mével, Ch. Dorrer, C. Le Blanc, F. Salin, and P. Agostini, *Optimizing High Harmonic Generation in Absorbing Gases: Model and Experiment*, Phys. Rev. Lett. **82**, 1668 (1999)
[37] D. Anderson, A. V. Kim, M. Lisak, V. A. Mironov, A. M. Sergeev, and L. Stenflo, *Self-sustained plasma waveguide structures produced by ionizing laser radiation in a dense gas*, Phys. Rev. E **52**, 4564–4567 (1995)